CHEMICAL & BIOMEDICAL IMAGING

Open Access

This article is licensed under CC-BY-NC-ND 4.0

pubs.acs.org/ChemBioImaging

Article

Fluorescence-Based Microviscosity Mapping in Membraneless Organelles

Avantika Kapoor, Pascal Didier,* Carla Faivre, Chloé Frey, Pierre Hener, Tania Steffan, Thiebault Lequeu, Andrey S. Klymchenko, Nicolas Anton, Mayeul Collot,* and Halina Anton*

Cite This: https://doi.org/10.1021/cbmi.6c00048

Read Online

ACCESS | Metrics & More | Article Recommendations | Supporting Information

ABSTRACT: Membraneless organelles (MLOs) are cellular biomolecular condensates formed by liquid−liquid phase separation. Their biological functions are intimately linked to their material properties, including viscosity. Condensate viscosity is determined by the size, shape, concentration, and molecular interactions between MLO components. It impacts the diffusion of MLO constituents and the selective permeability of the condensate, thereby regulating the rate of biochemical reactions. Viscosity modifications associated with the liquid-to-gel transition of the condensates are related to pathologies. Current experimental approaches for characterizing the material properties of cellular condensates remain limited. In this study, we report the use of BODIPY-based molecular rotors, in combination with fluorescence lifetime imaging microscopy (FLIM), to monitor the microviscosity of cellular MLOs directly in living cells. The fluorescence lifetime of BODIPY derivatives increases with the viscosity of their microenvironment, enabling a quantitative assessment of microviscosity within condensates. HaloTag technology was employed to specifically label MLO components. Our findings reveal that the nucleolus exhibits higher apparent viscosity than the surrounding nucleoplasm and that microviscosity varies across nucleolar subcompartments. Furthermore, nucleolar reorganization induced by the inhibition of rRNA synthesis results in a measurable increase in microviscosity. Finally, we demonstrate that the apparent microviscosity of stress granules is lower than that of the nucleoli. Overall, the presented results demonstrate the strong potential of BODIPY-based molecular rotors as versatile and powerful tools for probing local microviscosity in cellular membraneless organelles.

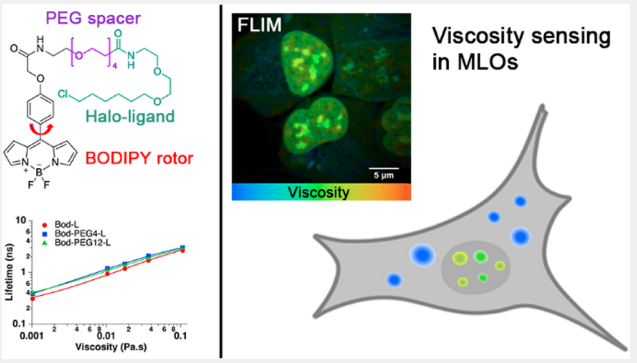

KEYWORDS: *membraneless organelles, viscosity probes, LLPS, BODIPY, FLIM*

INTRODUCTION

Liquid−liquid phase separation (LLPS) has recently emerged as a fundamental mechanism underlying cellular organization, driving the formation of biomolecular condensates, lipid membrane domains, and selective barriers.[1] LLPS is a thermodynamically driven, reversible process in which components of a homogeneous solution demix to form dense liquid condensates dispersed within a dilute phase. In cells, LLPS gives rise to organelles called membraneless organelles (MLOs), such as stress granules, P-bodies, Cajal bodies, or nucleolus.[2,3]

MLOs are complex, heterogeneous condensates that behave like fluids: they fuse, coalesce, and drip, which are behaviors governed by their physicochemical characteristics (i.e., surface tension, viscosity, etc). Because of their LLPS nature, MLOs represent transient, dynamic, and open systems whose biological functions are tightly linked to their composition, architecture, and material properties. These parameters are of crucial importance as the internal environment of condensates must be precisely regulated to fulfill their biological roles.[4]

Viscosity is one of the key physicochemical properties of molecular condensates. Viscosity represents the resistance of a fluid to flow. On a molecular scale, this property is determined by the concentration, size, shape, and interactions of the fluid's components. In MLOs, viscosity is particularly important because it affects internal dynamics and diffusion of their components. Condensate viscosity regulates the interfacial properties responsible for the droplet shape and the selective permeability which in turn impacts the rate of biochemical reactions. Under certain conditions, MLOs may undergo further phase transitions into gel-like or solid states, which are often associated with pathologies.[5] Therefore, understanding

Received: February 19, 2026
Revised: June 29, 2026
Accepted: June 29, 2026

ACS Publications

© XXXX The Authors. Co-published by Nanjing University and American Chemical Society

Downloaded from pubs.acs.org/cbihbp/article-pdf/doi/10.1021/cbmi.6c00048/6090427/cbmi.6c00048.pdf by guest on 07 September 2026

the relationship between biological function and the viscoelastic properties of MLOs remains a major challenge.

Several experimental approaches have been developed to probe condensate rheology at different scales. Passive microrheology, based on tracking fluorescent beads within reconstituted droplets, enables viscosity quantification in controlled environments, while droplet coalescence dynamics provide complementary estimates of interfacial tension and viscosity.[6] Active microrheology using optical tweezers further allows direct measurement of viscoelastic properties by applying oscillatory forces to embedded particles.[7−10]

Compared to "in vitro" systems, viscosity measurements in cellular condensates are more fastidious. In living cells, fluorescence recovery after photobleaching (FRAP) has been widely used to assess component mobility and infer viscosity from diffusion parameters.[11,12] More recently, optical diffraction tomography, a label-free imaging technique exploiting refractive index contrast, has been applied to quantify condensate density.[13,14] Together, these approaches have expanded our understanding of condensate material states, yet mapping viscosity at the nano to microscale within living cells remains challenging.

In this work, we introduce a complementary method for measuring the microviscosity within cellular condensates. We designed and optimized a BODIPY-based molecular rotor compatible with fluorescence lifetime imaging microscopy (FLIM), enabling direct, quantitative readout of local microviscosity. BODIPY dyes are environment-sensitive fluorophores, also called "molecular rotors" whose excited-state relaxation depends on their environment. In low-viscosity media, energy relaxation occurs via nonradiative intramolecular rotation, whereas in viscous environments, restricted motion leads to increased fluorescence quantum yield and lifetime. BODIPY-based rotors have already demonstrated high sensitivity for probing viscosity in cellular compartments such as the plasma membrane, mitochondria, and endoplasmic reticulum,[15−19] as well as in protein aggregates.[20] However, their potential for investigating cellular MLOs has remained unexplored.

To address this gap, we developed a chemogenetic labeling strategy based on a BODIPY derivative functionalized with a chloroalkane ligand for covalent conjugation to HaloTag-fusion proteins.[21] This approach enables the selective labeling of condensate components and the direct measurement of local viscosity in living cells. Using this tool, our experiments revealed distinct viscosity distributions within nucleolar subcompartments and dynamic changes accompanying nucleolar reorganization upon the inhibition of rRNA transcription. Furthermore, we identified significant viscosity differences between nucleoli and stress granules, reflecting their distinct internal architectures. Together, these findings establish BODIPY-based molecular rotors as powerful tools for live-cell imaging of microviscosity in biomolecular condensates, offering new insights into the material properties that underlie cellular organization.

MATERIALS AND METHODS

Chemicals and Synthesis

All starting materials were purchased from Sigma-Aldrich, BLD Pharm, or TCI Europe and were used as received, unless otherwise stated.

NMR spectra were recorded on a Bruker Avance III 400 MHz spectrometer. Chemical shifts (δ) are reported in ppm relative to residual solvent signals. High-resolution mass spectra were acquired using an Agilent Q-TOF 6520 mass spectrometer. Detailed synthetic protocols and full characterization of all compounds are provided in the Supporting Information (Figures S1−20).

Preparation of Glycerol−Water Mixtures for Rotor Calibration

To calibrate the viscosity sensitivity of the BODIPY-based rotor, a series of glycerol−water mixtures with different viscosities were prepared. Glycerol (Euromedex, France) and ultrapure Milli-Q water were mixed with defined mass ratios to achieve final glycerol percentages (w/w) of 0%, 35%, 45%, 60%, 67%, 72%, 75%, 77%, 82%, 85%, 90%, and 95%. Glycerol mixtures with 10 mM Tris and 150 mM NaCl at pH 7.5 were prepared to assess the influence of protein binding under physiological buffer conditions. The viscosity of each solution was measured at 20 °C using a HAAKE MARS rotational rheometer (Thermo Scientific, Waltham, MA, USA) equipped with a 35 mm parallel-plate geometry (P35/Ti/SB) set to a 0.10 mm gap and operated with a solvent trap to minimize evaporation. Approximately 100 μL of sample was loaded onto the lower plate and allowed to equilibrate at 20 °C prior to measurement. Steady-shear flow curves were acquired in controlled shear-rate mode, applying shear rates from 0.1 to 1000 s^{-1} and recording the corresponding shear stress. The apparent viscosity was calculated as $\eta = \tau/\dot{\gamma}$ (where $\dot{\gamma}$ is the shear rate and τ the shear stress) and, for such Newtonian mixtures, was taken from the shear-rate-independent plateau. Measurements were performed in triplicate.

Fluorescence Quantum Yield Measurements

The quantum yield (QY) of the BODIPY-COOH was measured for G0%, G45%, G67%, G77%, G85%, and G95% using the integrating sphere (SC-30) module of the FS5 fluorometer from Edinburgh Instruments. This module allows to determine the absolute fluorescence quantum yield of the dye. A dye concentration of 500 nM was used in a total sample volume of 4 mL. The sample was heated overnight at 50 °C to allow the dye to mix properly at high viscosity (i.e., G77%, G85%, and G95%). The excitation wavelength was set to 430 nm, and the emission was recorded from 440 to 700 nm.

Fluorescence Lifetime Measurements

Time-resolved fluorescence measurements were performed with the time-correlated single-photon counting technique. Excitation pulses at 500 nm were generated by a supercontinuum laser (NKT Photonics SuperK Extreme) with a 10 MHz repetition rate. The fluorescence decays were collected at 520 nm using a polarizer set at the magic angle and a 16 mm band-pass monochromator (Jobin Yvon). The single-photon events were detected with a microchannel plate photomultiplier R3809U Hamamatsu, coupled to a pulse preamplifier HFAC (Becker-Hickl GmbH) and recorded on a time-correlated single-photon counting board SPC-130 (Becker-Hickl GmbH). The measured decays were fitted by using a function corresponding to an exponential decay convolved with a normalized Gaussian curve of standard deviation σ standing for the temporal IRF and a Heaviside function. The fitting function was built in Igor Pro (Wavemetrics). All emission decays were fitted using a weighting that corresponds to the standard deviation of the photon number's square root.

Glycerol−water solutions were incubated at room temperature overnight to ensure homogeneity. A stock solution of 200 μM BODIPY rotors was prepared in DMSO. For each glycerol−water mixture, the BOD-L, BOD-PEG4-L, and BOD-PEG12-L rotors were added to achieve a final concentration of 50 nM. The experiments with HaloTag protein were performed in TRIS buffer (and corresponding glycerol mixtures) with the composition of the SEC equilibration buffer (10 mM Tris, pH 7.5, 150 mM NaCl) in order to preserve the protein conformation. This buffer is called TRIS in the following sections.

Cell Culture

Human embryonic kidney (HEK293) cell lines and Human bone osteosarcoma epithelial cell lines (U2OS) were used for live-cell

Downloaded from pubs.acs.org/cbihbp/article-pdf/doi/10.1021/cbmi.6c00048/6090427/cbmi.6c00048.pdf by guest on 07 September 2026

https://doi.org/10.1021/cbmi.6c00048
Chem. Biomed. Imaging XXXX, XXX, XXX−XXX

imaging experiments. HEK293 cells were grown in Dulbecco's Modified Eagle Medium (DMEM, Gibco) supplemented with 10% fetal bovine serum (FBS), 100 μg/mL penicillin, streptomycin, 2 mM L-glutamine, and 1 mM sodium pyruvate. U2OS cells were grown in modified Mc'Coy media containing 10% FBS, 100 μg/mL penicillin, streptomycin, and 1 mM sodium pyruvate. All cell lines were cultured at 37 °C in a humidified atmosphere containing 5% CO_2.

For fluorescence imaging, cells were seeded onto 35 mm Ibidi ibi-treat or glass-bottom dishes. HEK293 cells were seeded at a density of 1.5×10^5 cells/dish in 2 mL, while U2OS cells were seeded at a density of 5×10^4 cells/dish in 2 mL of their respective culture media. 24 h after seeding, cells were transfected with plasmid DNA using JetPEI (Polyplus, France) according to manufacturer's instructions.

Cloning

pcDNA-NPM-HaloTag[22] and pcDNA-Fib-HaloTag were cloned from GFP-NPM (Addgene no.: 17578) kindly provided by Dr. Wang[23] and peGFP-C1-Fib (Addgene no.: 26673) provided by Dr. Chen.[24] The HaloTag coding sequence was amplified from the pSEMS-Halo7Tag-hFis (Addgene no.: 111136) vector provided by Dr. Karin Busch.[25] After column purification, the PCR product was digested by *Bam*HI/XhoI restriction enzymes and inserted into the pcDNA3.1 (zeo) vector to obtain pcDNA-HaloTag. The NPM or Fib coding sequences were amplified from eGFP-NPM and eGFP-Fib plasmids, respectively, and inserted in *Hin*dIII/*Bam*HI pcDNA-HaloTag restriction sites to obtain the final pcDNA-NPM-HaloTag or pcDNA-Fib-HaloTag. All the constructs were verified by sequencing at Eurofins.

Fib-SNAP plasmid was generously provided by Dr. Castano.[26] and HaloTag-G3BP1 by Dr. Brandt's lab.[27] Plasmids coding for eGFP1 and eGFP3 were provided by Dr. Nalaskowski.[28] Plasmids coding for free HaloTag, HaloTag-H2B, and HaloTag-LifeAct were kindly provided by Dr. Gautier.[29]

Inhibition of RNA Pol 1 was performed by incubating the cells for 2 h in complete medium containing 2 μg/mL Actinomycin D. The stress granules formation was induced by the addition of 500 μM $NaAsO_2$ into the complete growth medium for 1 h. Cellular RNAs were stained by Pyronin Y (1 μM, 15 min, 37 °C). Actinomycin D, $NaAsO_2$, and Pyronin Y were purchased from Sigma-Aldrich.

Janelia Fluor dyes coupled to Halo and Snap ligands were provided by Janelia Materials (HHMI Janelia Research Campus).

Fluorescence Lifetime Imaging

Approximately 24 h post-transfection, the growth media was replaced with Opti-MEM (Gibco), and cells were incubated with 200 nM of BODIPY dyes for 15−20 min at 37 °C. Excess dye was removed by washing with Opti-MEM. For FLIM imaging of the calibration solutions, TRIS/glycerol mixtures containing 200 nM BOD-PEG4-L, either free or preincubated with a 5-fold molar excess of HaloTag protein, were loaded into Lab-Tek 8-well chambered coverglasses (Thermo Fisher Scientific).

FLIM measurements were performed on a Leica Stellaris microscope equipped with a FALCON module and on a homemade two-photon scanning FLIM microscope.

Commercial inverted confocal laser scanning microscope (STELLARIS 8, Leica Microsystems, Nanterre, France) was equipped with a fully fast integrated FLIM module, the so-called FAst Lifetime CONtrast (FALCON, Leica Microsystems, Nanterre, France) and a white light laser (WLL2 440−790 nm). Acquisitions were performed through a 512 × 512 image format, a scan speed of 400 Hz, and a 63× (NA 1.4) oil immersion objective. Bod-PEG4-L imaging was performed with 488 nm excitation (WLL, 8% power). In photon counting mode, a hybrid PMT HyD-X detector was used to detect fluorescence emission from 505 to 750 nm. FLIM images were acquired with the accumulation of 8 lines and 3 frame repetitions to detect ∼1000 photons in each pixel showing Bod-PEG4-L labeled structures. A minimum of 100 photons was set for pixels represented in the phasor plot.

The homemade multiphoton scanning microscope is based on an inverted microscope (IX83, Olympus) with a 60× 1.2 NA water immersion objective operating in the descanned fluorescence collection mode.[30] The BODIPY derivatives were excited at 780 nm using a femtosecond laser (Insight DeepSee, Spectra Physics). Fluorescence photons were collected at a dwell time of 4 μs/pixel using a short-pass filter with a cutoff wavelength of 720 nm (Semrock, FF01−720/SP-25). The fluorescence was directed to a fiber-coupled APD (SPCM-AQR-14-FC, PerkinElmer), which was connected to a time-correlated single-photon counting module (SPC830, Becker & Hickl). The measurements were controlled by SPCM ver. 9.83 (Becker & Hickl). The time-resolved fluorescence decay at each pixel was analyzed using SPC Image FLIM analysis software package (Becker & Hickl). FLIM images were acquired by scanning the sample for 90−120 s with a typical laser power of 0.75 mW on the microscope stage to detect a minimum of 3000 photons per pixel. The decay curves were fitted using a biexponential model, convolved with the instrument response function (IRF), as

$$I(t) = IRF \otimes (A_1 e^{-t/\tau 1} + A_2 e^{-t/\tau 2})$$

where $I(t)$ represent the intensity decay and IRF denotes the instrument response function of the system. A_1 and A_2 are the amplitudes of the two decay components with τ_1 and τ_2 fluorescence lifetimes. The average fluorescence lifetime τ was then calculated as

$$\tau = \frac{\tau_1 \times A_1 + \tau_2 \times A_2}{A_1 + A_2}$$

Pixel-wise fitting was carried out to generate fluorescence lifetime maps, and regions of interest (ROIs) were selected to extract quantitative data for comparison across the experimental conditions. Several BOD-PEG4-L solutions in water/glycerol mixtures were analyzed by both FLIM and cuvette-based TCSPC to ensure that the absolute lifetime values obtained by the two techniques are consistent (Figure S21).

Phasor Analysis

Phasor analysis is a fit-free technique in which the fluorescence decay from each pixel is transformed into a point in two-dimensional (2-D) phasor space.[31,32] If $P(i,j)$ represents a pixel in the FLIM image with coordinates (i,j) and $I_{i,j}(t)$ is the fluorescence intensity decay at that pixel, the corresponding coordinates in the phasor plot (g,s) for time-domain measurements are given as

$$g_{i,j}(\omega) = \frac{\int_0^T I_{i,j}(t)\cos(\omega t)dt}{\int_0^T I_{i,j}(t)dt}$$

$$s_{i,j}(\omega) = \frac{\int_0^T I_{i,j}(t)\sin(\omega t)dt}{\int_0^T I_{i,j}(t)dt}$$

where $\omega = 2\pi f$ and $f = 1/T$ is the laser repetition rate. Phasor analysis provides a visual distribution of the molecular species in an image by clustering pixels with similar lifetimes. Phasor plots were generated by phasor-FLIM analysis using Leica LAS X Navigator and SPC Image (Becker & Hickl). The raw phasor data were exported and plotted by using R (R Foundation for Statistical Computing, Vienna, Austria).

Recombinant Protein Production

Recombinant HaloTag protein with an N-terminal 6×-His tag was purified using the *E. coli* expression system, BL21(DE3) cells. Competent bacteria were transformed with the pET28-Halo plasmid, and protein expression was induced by adding 500 μM IPTG. After 4 h of culturing, the cells were centrifuged and the pellet was conserved at −80 °C. For the purification, the cells were lysed by ultrasonication: 2 s ON, 2 s OFF (1 min/mg of dry pellet), 17 W/wave, in Lysis buffer (20 mM Tris−HCl, pH 7.5, 150 mM NaCl, 10 mM imidazole, 5 mM β-mercaptoethanol, 1 mM PMSF, and a protease inhibitor mixture (Roche Diagnostics)), and then centrifuged at 20,000 × *g*, 4 °C for 45 min. The supernatant was filtered with 0.22 μm low-binding filters and loaded on a Ni-NTA agarose column (Qiagen) beforehand equilibrated with Equilibration Buffer (20 mM Tris−HCl, pH 7.5, 500 mM NaCl, 15 mM imidazole). HaloTag protein was eluted with Ni-Elution buffer (20 mM Tris, pH 7.5, 500

Downloaded from pubs.acs.org/cbihbp/article-pdf/doi/10.1021/cbmi.6c00048/6090427/cbmi.6c00048.pdf by guest on 07 September 2026

https://doi.org/10.1021/cbmi.6c00048
Chem. Biomed. Imaging XXXX, XXX, XXX−XXX

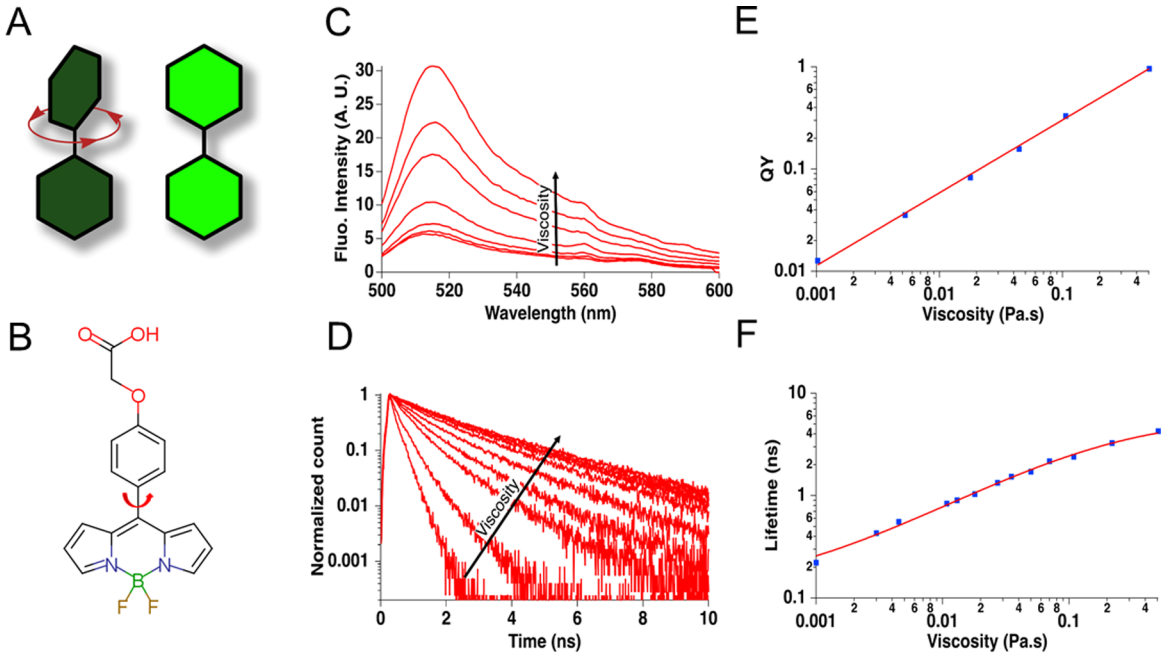

Figure 1. (A) Rotational mechanism of BODIPY-based molecular rotors; (B) structure of BOD-COOH; (C) the fluorescence emission spectra and (D) fluorescence decay curves of BOD-COOH in water/glycerol mixtures with increasing viscosities. (E–F) Förster–Hoffmann plots of fluorescence quantum yield and lifetime vs viscosity (blue squares correspond to the data points and the continuous red lines to the fit obtained using eqs 1 and 2).

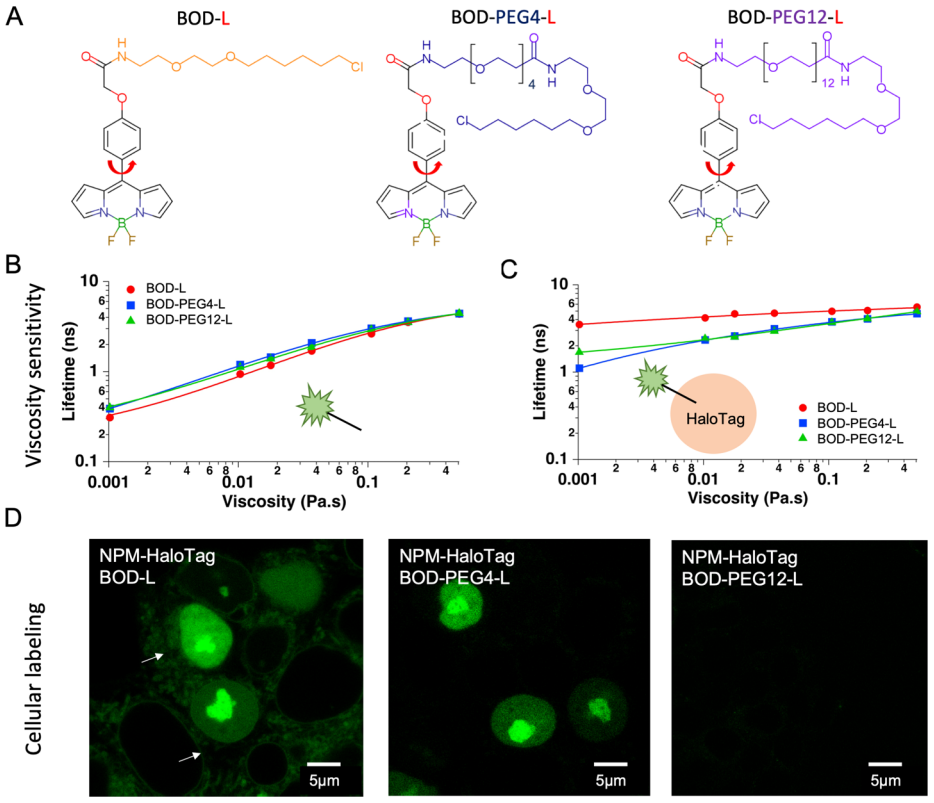

Figure 2. (A) Structures of BOD-L, BOD-PEG4-L, and BOD-PEG12-L derivatives. (B) Fluorescence lifetimes measured for the BODs alone (50 nM) (individual points correspond to data points and the continuous line to the fit obtained using eq 2) and (C) in the presence of HaloTag protein (0.5 μM) (individual points correspond to data points and the continuous line to the fit obtained using eq 2). For both conditions, the alpha values are reported in the main text. (D) HEK293 cells expressing NPM-HaloTag labeled with BODIPY chloralkane derivatives. BOD-L labels specifically the cell nucleolus; however, a slight cytoplasmic signal is also present. Cells labeled with BOD-PEG4-L show only specific probe binding to the NPM-HaloTag. For BOD-PEG12-L, no fluorescence was detected in the cells.

Downloaded from pubs.acs.org/cbihbp/article-pdf/doi/10.1021/cbmi.6c00048/6090427/cbmi.6c00048.pdf by guest on 07 September 2026

https://doi.org/10.1021/cbmi.6c00048
Chem. Biomed. Imaging XXXX, XXX, XXX–XXX

mM NaCl, and 1000 mM imidazole). Elution from Ni-NTA was concentrated to 2 mL (Amicon Ultra 4, 10K, Millipore) and loaded into a size exclusion chromatography column (SEC) beforehand equilibrated with SEC Equilibration Buffer (10 mM Tris, pH 7.5,150 mM NaCl, 2 mM DTT). Fractions containing the HaloTag protein were pooled, concentrated to ∼50 μM, and aliquots were flash-frozen in liquid nitrogen and stored at −80 °C for 1−6 months. The integrity of the HaloTag protein before and after storage was verified by Coomassie-stained gel electrophoresis (Figure S22).

RESULTS

BODIPY-Derived Molecular Rotors Are Sensitive to Viscosity

BODIPY-based molecular rotors display absorption and emission maxima centered at 480 and 520 nm, respectively. The de-excitation pathways of these molecules depend on conformational flexibility and the rotational freedom of their phenyl moiety (Figure 1A,B). In viscous environments, where molecular mobility is restricted, radiative relaxation is favored, resulting in an increase in both fluorescence quantum yield and lifetime. Hence, we first characterized the viscosity response with a water/glycerol mixture of varying viscosity by measuring the fluorescence quantum yield (Φ_F) of the BODIPY-COOH (BOD-COOH) derivative. The viscosities (η) of the mixtures were systematically determined using an oscillatory rheometer. The relationship between τ, Φ_F, and η follows the Förster−Hoffmann model:

$$\phi = A \cdot \eta^{\alpha} \tag{1}$$

where A is a constant and α reflects the sensitivity of the molecular rotor to viscosity. The viscosity values ranged from 1 mPa·s for pure water to 506 mPa·s for 95% glycerol at 20 °C. As shown in Figure 1C and 1E, the fluorescence quantum yield increased with environmental viscosity, following the Förster−Hoffmann relationship with α values of 0.71 ± 0.02. We next measured the time-resolved fluorescence decays of the same water/glycerol mixtures. In line with the quantum yield measurements, upon an increase in viscosity, the fluorescence lifetime of the BOD-COOH derivative increased (Figure 1D and 1F). To account for the variation of the lifetime as a function of viscosity, we used a model previously described by Vyšniauskas et al.:[33]

$$\tau = \frac{1}{\frac{A}{B \cdot \eta^{\alpha} + C} + D} \tag{2}$$

where A, B, C, and D are unconstrained parameters that account for intrinsic lifetime measured at zero viscosity (C), the radiative lifetime of the dye (without a nonradiative relaxation pathway) (D), and the activation energy associated with the rotation of the phenyl moiety (A) and the constant from the Förster−Hoffmann model (B). α reflects the sensitivity of the molecular rotor to viscosity and was fixed to the value obtained from the quantum yield analysis.

To specifically target the BODIPY rotor to components of MLOs, we employed a HaloTag labeling strategy. A chloroalkane HaloTag ligand was directly conjugated to the fluorophore or linked via polyethylene glycol (PEG) spacers of 4 or 12 units (Figure 2A). The PEG linkers increase the distance between the BODIPY rotor and the binding site within the HaloTag binding pocket, thereby minimizing the influence of the protein environment on viscosity sensing.

Control experiments were performed before the fluorescence lifetime measurements. Since probe aggregation was observed in water and TRIS buffer at concentrations around 1 μM, all TCSPC measurements in cuvettes were performed at a 50 nM concentration. The HaloTag binding experiments were conducted in the presence of a 5−10-fold excess of protein to ensure complete probe binding. The specificity of halo ligand binding to the HaloTag protein was first verified by fluorescence anisotropy and FCS measurements by using the JF552-HaloLigand dye. These measurements confirmed the presence of a single fluorescent species, with a rotational correlation time consistent with a molecular weight of 36.5 kDa (HaloTag M_w = 33 kDa) (Figure S23). FCS further confirmed a 1:1 labeling and complete dye binding (Figure S24). Together, these results demonstrate that the HaloTag protein remains properly folded, binds its ligand specifically, and that under the conditions used for the calibration, the dye is fully bound to the protein.

The time-resolved fluorescence decays of BOD-L, BOD-PEG4-L, and BOD-PEG12-L were measured to retrieve their fluorescence lifetimes as a function of the viscosity of water/glycerol mixtures without (Figure 2B, raw decays in Figure S25) and in the presence of the purified HaloTag protein (Figure 2C and Figure S25). As shown in Figure 2B, all three BODIPY derivatives retained viscosity sensitivity $\alpha_{BOD\text{-}L}$ = 0.71 ± 0.04, $\alpha_{BOD\text{-}PEG4\text{-}L}$ = 0.64 ± 0.03, $\alpha_{BOD\text{-}PEG12\text{-}L}$ = 0.65 ± 0.04). Notably, the viscosity sensitivity of BOD-L was strongly reduced upon HaloTag binding (Figure 2C), suggesting that the fluorophore remained too constrained by the protein environment to efficiently sense changes in the surrounding medium ($\alpha_{BOD\text{-}L+HaloTag}$ = 0.07 ± 0.01). In contrast, both BOD-PEG4-L and BOD-PEG12-L exhibited similar viscosity-dependent fluorescence responses, although their sensitivity was slightly reduced compared to the unbound fluorophores ($\alpha_{BOD\text{-}PEG4\text{-}L+HaloTag}$ = 0.29 ± 0.02, $\alpha_{BOD\text{-}PEG12\text{-}L+HaloTag}$ = 0.35 ± 0.05). This reduction suggests that rotational restriction imposed by the protein environment partially affects the fluorophore's relaxation.

Of note, the presented BOD derivatives do not possess a pronounced donor−acceptor structure or an intramolecular charge-transfer (ICT) architecture, unlike classical polarity-sensitive solvatochromic dyes. Therefore, their fluorescence lifetime is expected to be governed primarily by the restriction of intramolecular rotation and to exhibit limited sensitivity to changes in environmental polarity.[33] In addition, the ionic strength of the medium does not appear to significantly affect the fluorescence lifetime of the probe. Indeed, the fluorescence decay profiles of BOD-PEG4-L measured in pure water and in TRIS buffer (10 mM TRIS, 150 mM NaCl) were nearly identical (Figure S26), indicating a negligible influence of ionic strength under the conditions used in this study.

Finally, it should be noted that the present approach measures the microviscosity, i.e., the viscosity of the environment in the immediate vicinity of the rotor. Molecular rotors are sensitive to viscosity generated by small solutes such as glycerol, sucrose, or short PEG chains, but become progressively insensitive when viscosity mainly arises from larger polymeric structures and longer-range interactions (long PEG chains (>1000)).[15] As shown in Supplementary Figure S27 which presents the viscosity sensitivity of BOD-COOH in solutions with PEGs of various molecular weights, the correlation between microviscosity measured with the rotor and macroviscosity measured by rheometry decreases with

Downloaded from pubs.acs.org/cbihbp/article-pdf/doi/10.1021/cbmi.6c00048/6090427/cbmi.6c00048.pdf by guest on 07 September 2026

https://doi.org/10.1021/cbmi.6c00048
Chem. Biomed. Imaging XXXX, XXX, XXX−XXX

increasing PEG hydrodynamic radius and is essentially lost for PEGs with a hydrodynamic radius above ~2 nm. Therefore, the calibration curves established in simple glycerol/water mixtures should be interpreted as providing local microviscosity estimates rather than absolute macroscopic rheological values.

We next evaluated the three BODIPY probes for their ability to label HaloTag-fusion proteins in living cells. HEK293 cells expressing the nucleolar protein Nucleophosmin-1 fused to HaloTag (NPM-HaloTag) were labeled and imaged by confocal microscopy (Figure 2D). BOD-L produced a strong fluorescence signal within the nucleolus but also exhibited substantial nonspecific staining in the cytoplasm. In contrast, BOD-PEG4-L selectively labeled the nucleolus with minimal background fluorescence. No significant intracellular signal was detected for the BOD-PEG12-L derivative, which likely failed to penetrate the cells because of the increased hydrophilicity conferred by the long PEG12 linker.

In light of these results, all cellular experiments in this study were performed with BOD-PEG4-L.

BOD-PEG4-L Senses the Viscosity in Various Cellular Compartments

To assess the sensitivity of the BOD-PEG4-L rotor to microviscosity within the cellular environment, different subcellular structures in U2OS cells were labeled by expressing specific HaloTag-fusion proteins: free cytoplasmic HaloTag protein, HaloTag-H_2B in the cell nucleus, LifeAct-targeting HaloTag to actin filaments, and HaloTag-hFis1 in mitochondria. The autofluorescence signal of unlabeled cells was negligible, and the nonspecific labeling (mainly cytoplasmic) was observed only for the BOD-L probe (Figure S28).

We evaluated the effect of light illumination on the BOD-based viscosity probes. It was previously reported that a BODIPY derivative very similar to our probe BOD-PEG4-L induces photobleaching of the labeled HaloTag protein, resulting in a significant increase in fluorescence lifetime upon repeated FLIM imaging.[34] To assess this effect, we acquired 17 consecutive FLIM images of the same region and did not observe any significant increase in fluorescence lifetime under classical excitation conditions (Figure S29A).

We then increased the laser power to 2.25 mW, reduced the scanning speed, and restricted imaging to a smaller region. Under these conditions, a clear increase in fluorescence lifetime (τ) was observed (Figure S29B). Importantly, this increase in τ was also observed after illumination with an 488 nm LED source, either at high intensity or over extended periods (Figure S29C).

The same experiments were performed with the BOD-L probe. The fluorescence lifetime was already higher compared with that of BOD-PEG4-L and remained constant even under high-intensity illumination.

Altogether, these results indicate that, prior to using BOD-based molecular rotors, it is essential to carefully assess the influence of illumination conditions and to minimize light exposure.

We next performed the FLIM measurements in U2OS cells expressing HaloTag targeted to different cellular compartments. Acquired FLIM images were analyzed by decay fitting and phasor plot analysis. The phasor approach offers a fit-free, intuitive way to analyze lifetime data by converting the measured fluorescence decay in each pixel of the image into a point (vector) in a 2D plot using a Fourier transform at the modulation frequency of the excitation source (see Materials and Methods section).[31,32] In the resulting phasor plot, the pixels are distributed on the half-circle with the shortest lifetimes plotted on the right side of the plot and longer lifetimes closer to the origin.[32]

Representative cellular phasor plots were compared with the calibration data obtained for BOD-PEG4-L (Figure S30A and B). The cellular phasor distributions were located close to the calibration trajectory, indicating that the mean lifetimes measured in cells remain consistent with the viscosity-dependent photophysical response of the HaloTag-bound rotor and that a possible impact of dynamic quenching of the probe is minimal under these experimental conditions. In addition, it is unlikely that the presented lifetime variations arise primarily from nonspecific molecular binding or macromolecular crowding effects. The fluorescence lifetime of BOD-PEG4-L was found to be insensitive to the presence of molecular crowders such as high-molecular-weight PEG (Figure S27), and closely related BODIPY-based molecular rotors have previously been shown to exhibit negligible sensitivity to protein-rich cellular extracts.[15] Therefore, the calibration curve presented in Figure 2C was used to estimate the apparent local microviscosities within the investigated cellular compartments.

As observed during the calibration measurements, the cellular fluorescence decays were best described by a biexponential model (Figure S30C and Table S5). The average fluorescence lifetime measured in the cytosol ($\tau_{cytosol}$ = 1.5 ns) corresponded to a low apparent microviscosity (2.4 mPa·s). Higher apparent microviscosities were observed in the chromatin ($\tau_{chromatin}$ = 2.3 ns, 10 mPa·s) and within the actin cytoskeleton (τ_{actin} = 2.5 ns, 14 mPa·s). The longest fluorescence lifetime was observed in the hFis1 protein located in the mitochondrial outer membrane ($\tau_{mitochondria}$ = 3.5 ns) corresponding to an apparent microviscosity of approximately 70 mPa·s.

Of note, because the cellular microenvironments are more heterogeneous than isotropic calibration solutions and may include additional photophysical contributions, the reported values should be interpreted as estimates of the apparent local microviscosities sensed in the vicinity of the labeled proteins and not as absolute macroscopic viscosity values of the corresponding cellular structures.

Low apparent viscosity in the cell cytoplasm ($\eta_{cyt} \approx 2.4$ mPa·s) correlates well with previous fluorescence correlation spectroscopy (FCS) studies.[35] Interestingly, this value is lower than that reported by Kuimova and collaborators for the BODIPY rotor lacking the targeted moiety.[15] The viscosity measured by the probe targeted to H_2B in the chromatin (η = 10 mPa·s) and actin fibers (η =14 mPa·s) was higher than that of the cytoplasm. These values are in good agreement with previously reported nuclear viscosity estimations.[36] In line with this, FCS studies reported reduced diffusion of monomeric eGFP in the nucleoplasm, by a factor of approximately 3.2 relative to aqueous solution,[36] corresponding to an estimated viscosity of 3−4 mPa·s. Our measurements corroborate the notion that chromatin is embedded within a low-viscosity aqueous phase permissive to the diffusion of low-molecular-weight proteins.

Fluorescence lifetimes recorded in mitochondria ($\tau \approx 3.5$ ns) were close to those reported by Chambers et al.,[15] although viscosity values inferred from calibration curves differed (325 mPa·s in[15] vs 71 mPa·s in our study). These

Downloaded from pubs.acs.org/cbihbp/article-pdf/doi/10.1021/cbmi.6c00048/6090427/cbmi.6c00048.pdf by guest on 07 September 2026

https://doi.org/10.1021/cbmi.6c00048
Chem. Biomed. Imaging XXXX, XXX, XXX−XXX

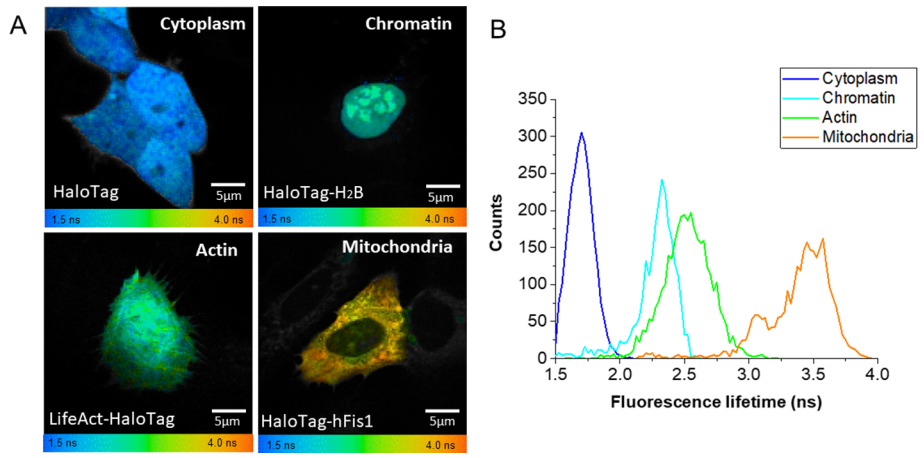

Figure 3. BOD-PEG4-L is sensitive to the environment in various cellular compartments: (A) FLIM images of cells expressing free HaloTag protein, HaloTag-H_2B fusion (chromatin labeling), HaloTag-LifeAct to label the actin fibers, and mitochondrial protein HaloTag-hFis1. (B) Corresponding fluorescence llifetimes distributions.

discrepancies may arise from differences in the specific mitochondrial proteins targeted (matrix versus outer membrane), which likely expose the probe to distinct local environments. Of note, our results are close to the microviscosity measured by the BODIPY-derived ratiometric mitochondrial probe (62 mPa·s).[37]

These data confirm that the sensitivity of the BOD-PEG4-L probe is conserved in cells and that FLIM imaging reports on the microviscosity of the environment in the proximity of the labeled proteins in various cellular organelles.

The loss of sensitivity of the BOD-L probe upon binding to the HaloTag protein (Figure 2) is surprising, given that a very similar probe was reported to be sensitive by the group of Kuimova.[15] To further investigate this discrepancy and complement the in vitro measurements, we tested the probe in living cells expressing HaloTag in different subcellular compartments. In agreement with the calibration data, the fluorescence lifetimes measured for NPM-HaloTag, free HaloTag, and H_2B-Halo were all close to 3.5 ns (Figure S28), further supporting the conclusion that the probe loses its sensitivity upon binding to HaloTag.

Mapping the Microviscosity in Different Subcompartments of the Nucleolus

BOD-PEG4-L tool was next used to map the viscosity properties of the cell nucleolus. The nucleolus is a 1−2 μm-sized MLO;[38] it is implicated in ribosomal biogenesis, cell cycle regulation, and the cellular stress response. The nucleolus is composed of three distinct compartments: the fibrillar centers (FC)—sites of rRNA transcription by RNA Pol 1; dense fibrillar component (DFC), where the rRNA is processed; and the granular component (GC) being a site of the preribosomal subunit assembly.[39]

To monitor the microviscosity in the nucleolar subcompartments, two nucleolar proteins, Nucleophosmin-1 (NPM) and Fibrillarin (Fib), were fused to HaloTag and expressed in HEK and U2OS cells. NPM and Fib are known to localize predominantly in GC and DFC, respectively, and are likely to contribute to their formation via liquid−liquid phase separation.[38,40] It has previously been reported that their fusion to eGFP does not impact their specific localization.[41,42] To verify whether the presence of the HaloTag or protein overexpression affected their localization, HEK293 and U2OS cells were cotransfected with both eGFP- and Halo-tagged versions of NPM and Fib and analyzed by confocal microscopy. As shown in Figure S31, Halo-tagged proteins showed strong colocalization with their eGFP-tagged counterparts in both cell lines, supporting their localization in GC and DFC, respectively.

Next, we performed FLIM imaging of NPM-HaloTag and Fib-HaloTag labeled with BOD-PEG4-L. Figure 4A represents intensity images and corresponding phasor plots for NPM-HaloTag and Fib-HaloTag proteins expressed in HEK293 cells. The phasor plots for each protein show an elongated shape enabling the selection of pixels from two populations with different lifetimes (Figure 4A, Phasor ROI and Phasor plot insets). When displaying the corresponding pixels on the FLIM images, these two populations represent NPM or Fib proteins located in the nucleoplasm (shorter lifetime) and in the nucleolus (longer lifetime).

Next, we performed TCSPC FLIM imaging to retrieve the fluorescence lifetimes by fitting the decays (Figure 4B and Table 1). Representative fluorescence decays together with the obtained lifetime components and phasor plots are presented in Figure S32 and Table S6. BOD-PEG4-L bound to the nucleolar NPM-HaloTag showed a lifetime τ_{NPM} = 1.97 ± 0.17 ns, corresponding to the apparent viscosity of 5.5 mPa·s. Interestingly, the environment within the DFC seems to be more viscous, lifetimes measured for Fib-HaloTag are significantly higher compared to NPM, τ_{Fib} = 2.43 ± 0.18 ns, η=12 mPa·s. For both nucleolar proteins examined, we found that the nucleolus exhibits significantly higher viscosity than the surrounding nucleoplasm. These trends were reproducible in the two cell lines tested HEK293 and U2OS.

Feric et al. showed by coalescence and FRAP measurements a liquid-like behavior for the GC and a more viscoelastic behavior for the DFC.[40] Our results confirm the distinct viscosity properties among nucleolar subdomains, underscoring the high sensitivity of BOD-PEG4-L to its local environment. Overall, apparent microviscosity values ranged from ∼5−8 mPa·s in the GC to ∼12−14 mPa·s in the DFC and appeared independent of the cell line examined. Our findings are consistent with nanoscale techniques such as FCS measurements of GFP diffusion in the nucleolus, which report diffusion coefficients reflecting a viscosity range of 4−26 mPa·s.[13,35,43] However, these values are considerably lower than

Downloaded from pubs.acs.org/cbihbp/article-pdf/doi/10.1021/cbmi.6c00048/6090427/cbmi.6c00048.pdf by guest on 07 September 2026

https://doi.org/10.1021/cbmi.6c00048
Chem. Biomed. Imaging XXXX, XXX, XXX−XXX

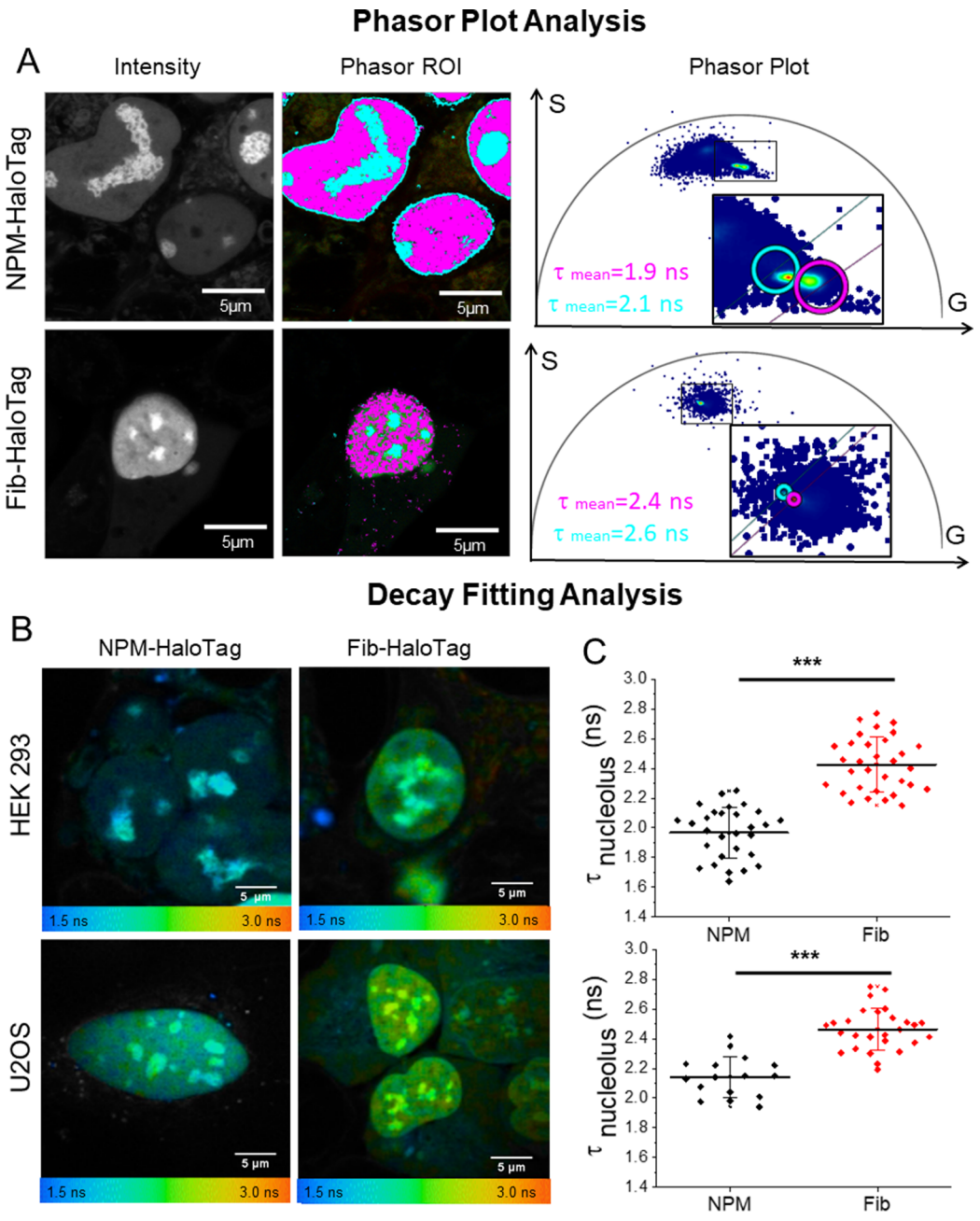

Figure 4. BOD-PEG4-L senses the microviscosity in nucleolar subcompartments: (A) intensity images, phasor plot, and ROI analysis of HEK293 cells expressing NPM-HaloTag or Fib-HaloTag labeled with BOD-PEG4-L. The phasor plot displays two populations with shorter lifetimes corresponding to the dye in the nucleoplasm and longer lifetimes for the dye present in the nucleolus. (B) FLIM images of HEK293 and U2OS cells expressing NPM-HaloTag and Fib-HaloTag. (C) Average lifetimes ± SD measured for 15−30 cells in each condition measured in 3 independent experiments. Data were analyzed using an unpaired two-tailed Student's t-test with unequal variances, ***$p < 0.001$.

Table 1. Mean Fluorescence Lifetimes ± SD Measured in Nucleolar Subcompartments and Corresponding Viscosity (η) Values[a]

Cell line	τ_{GC} (ns)	η (mPa·s)	τ_{GC} (ns) + ActD	η (mPa·s)	τ_{DFC} (ns)	η (mPa·s)	τ_{DFC} (ns) + ActD	η (mPa·s)
HEK293	1.97 ± 0.17	5.5	2.11 ± 0.10	7	2.43 ± 0.18	12	2.62 ± 0.25	16
U2OS	2.14 ± 0.14	7.5	2.28 ± 0.12	9.5	2.46 ± 0.14	13	2.65 ± 0.18	18

[a]Values based on 3 independent experiments with a total of 15−30 cells analyzed in each condition.

viscosity measurements reported for *in vitro* reconstituted condensates, 700 mPa·s.[40] Such differences stem from the distinct physical scales probed by each technique.

In this manuscript, *microviscosity* refers to viscosity arising from molecular-scale interactions, including intermolecular contacts, hydrogen bonding, and other short-range interactions, as well as their local concentration. As in fluorescence correlation spectroscopy (FCS), the sensitivity threshold of this approach is on the order of the probe molecule's correlation length.[44] By contrast, *macroviscosity* describes

Downloaded from pubs.acs.org/cbihbp/article-pdf/doi/10.1021/cbmi.6c00048/6090427/cbmi.6c00048.pdf by guest on 07 September 2026

https://doi.org/10.1021/cbmi.6c00048
Chem. Biomed. Imaging XXXX, XXX, XXX−XXX

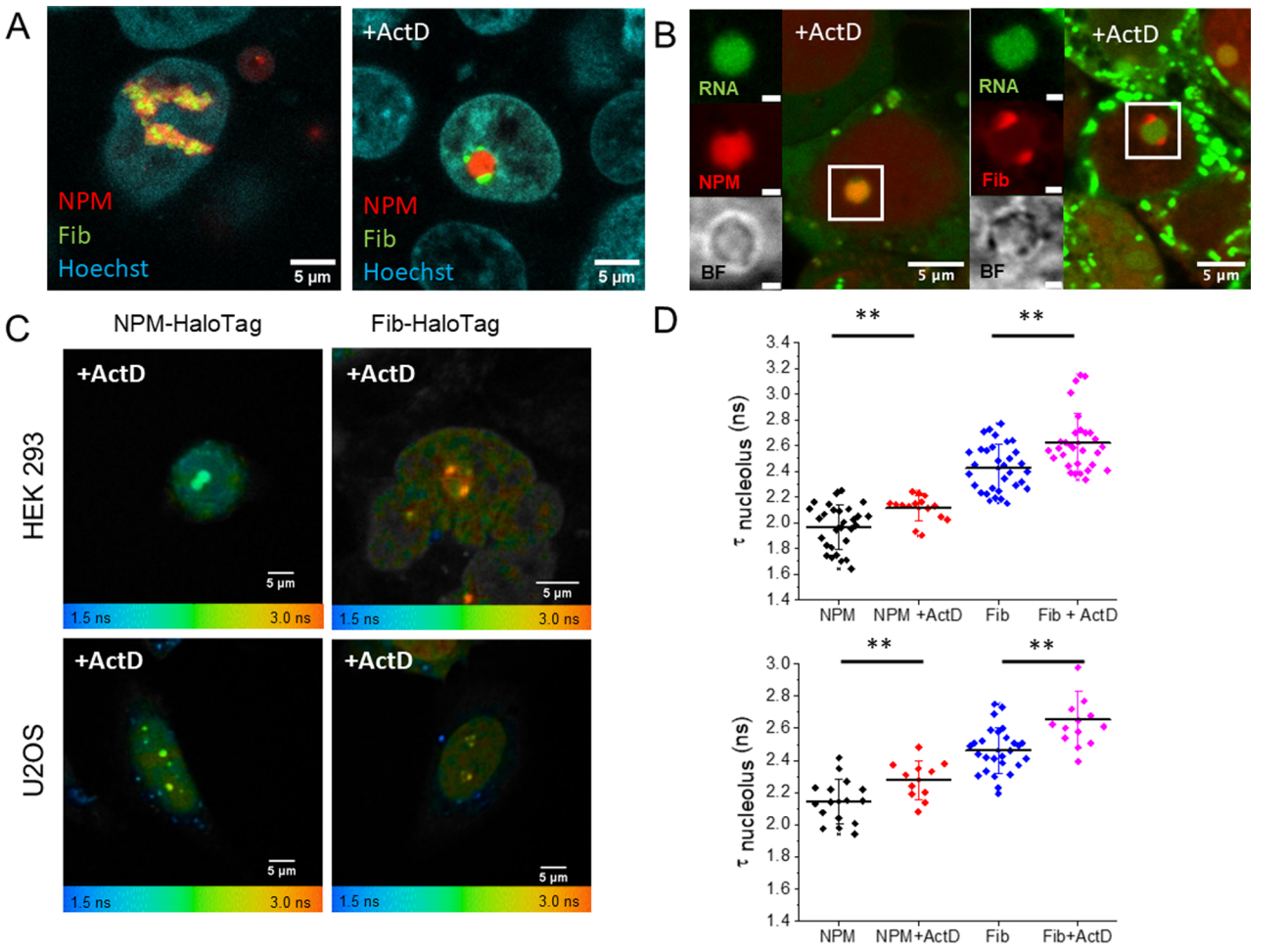

Figure 5. (A) Confocal images of HEK293 cells expressing NPM-HaloTag (JF657-Halo) and Fib-SNAP (JF552-SNAP). ActD treatment induces the separation of GC with DFC forming nucleolar caps on the surface. (B) Confocal images of ActD-treated HEK293 cells expressing NPM-HaloTag (JF657-Halo) or Fib-HaloTag (JF657-Halo) costained with Pyronin Y (1 μM, 15 min). (C) FLIM images of HEK293 and U2OS cells expressing NPM-HaloTag or Fib-HaloTag labeled with BOD-PEG4-L. (D) Mean fluorescence lifetimes ± SD. Values are based on 3 independent experiments with a total of 15−30 cells analyzed in each condition. Data were analyzed using an unpaired two-tailed Student's t-test with unequal variances $^{**}p < 0.01$.

material properties at larger (μm) length scales, where viscoelastic behavior emerges from large polymers and network formation. Accordingly, in biomolecular condensates, viscosity arises from both protein−protein interactions and larger-scale network organization. Consequently, micro- and macroscale measurements can differ substantially. For example, NPM condensates exhibit a viscosity of 700 mPa·s[40] by micro-rheology, whereas FCS and our measurements indicate a local viscosity approximately 10-fold lower.[13,35,43]

Finally, it should be noted that all measurements in this study were performed on asynchronous cell populations. Since the cell nucleolus disassembles before cell division and reassembles at the end of mitosis,[45,46] it is highly probable that the nucleolar viscosity varies during the cell cycle, and this question should be considered in future work.

Effect of rRNA Transcription Inhibition on Nucleolar Microviscosity

To test the sensitivity of the BOD-PEG4-L probe to the viscosity modifications induced by changes in the composition of the nucleolar subcompartments, we performed FLIM imaging of cells treated with Actinomycin D (ActD), an inhibitor of RNA polymerase I. In the treated nucleoli, the DFCs fused together and progressively migrated to the nucleolar periphery, where they formed structures called "nucleolar caps". Concomitantly, the GC became smaller and spherical, showing clearly its liquid-like properties (Figure 5A). These changes accompany the release of nucleolar proteins from their molecular complexes and alterations in their interactions with rRNA, leading to an increase in protein mobility and their partial relocalization to the nucleoplasm.[42] RNA imaging performed after 2 h of ActD treatment showed no presence of RNA in the nucleolar caps; however, a residual RNA signal was still detectable in GCs (Figure 5B). Therefore, the DFC changed from a protein/RNA condensate to a purely protein-rich condensate, while the impact on the GC composition was less pronounced.

To monitor the microviscosity changes accompanying this nucleolar reorganization, HEK293 and U2OS cells expressing NPM-HaloTag or Fib-HaloTag labeled with BOD-PEG4-L were treated with ActD.

Two-photon fluorescence lifetime imaging (FLIM) confirmed a clear morphological change in the nucleolus upon ActD treatment in both the HEK293 and U2OS cells. Lifetime measurements in ActD-treated cells revealed an increase in BOD-PEG4-L fluorescence lifetime in both subcompartments

Downloaded from pubs.acs.org/cbihbp/article-pdf/doi/10.1021/cbmi.6c00048/6090427/cbmi.6c00048.pdf by guest on 07 September 2026

https://doi.org/10.1021/cbmi.6c00048
Chem. Biomed. Imaging XXXX, XXX, XXX−XXX

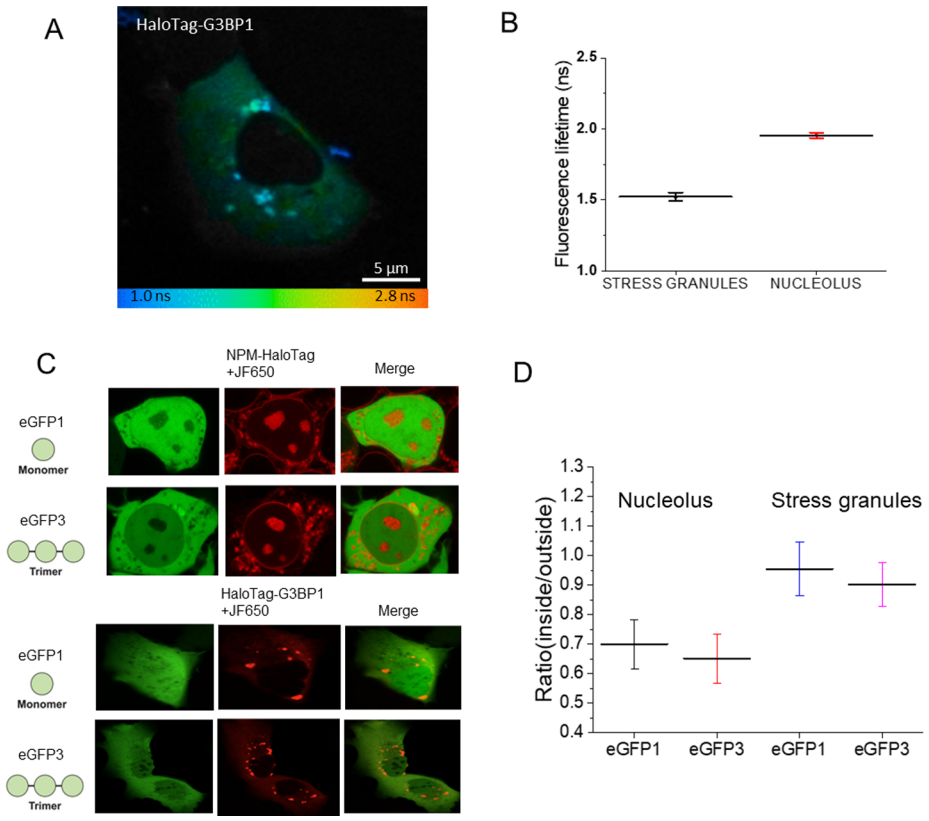

Figure 6. (A) FLIM image of U2OS cells expressing HaloTag-G3BP1 labeled with BOD-PEG4-L. Cells were treated with sodium arsenite (0.5 mM, 1 h) to induce the formation of stress granules. (B) Mean fluorescence lifetimes ± SD measured for NPM-HaloTag and HaloTag-G3BP1. Values are based on 3 independent experiments with a total of 15−30 cells analyzed in each condition. (C) Confocal images of HEK293 cells expressing NPM-HaloTag labeled by JF650-Halo ligand together with eGFP or eGFP3, and U2OS cells expressing HaloTag-G3BP1 labeled by JF650-Halo ligand together with eGFP or eGFP3. Scale bars: 5 μm. (D) Fluorescence intensity ratios of eGFP signal inside vs outside of both MLOs.

(Table 1, Figure 5C,D, Figure S32 and Table S6). The fluorescence lifetime for NPM-HaloTag increased by 0.14 and 0.15 ns in HEK293 and U2OS cells, respectively, corresponding to an apparent viscosity increase of around 2 mPa·s. Similarly, for the Fib-HaloTag, an increase of 0.19 and 0.20 ns was measured which reflects a viscosity increase of 4 mPa·s.

This observation confirms that the reorganization of the condensate's internal structure from an RNA-containing to an RNA-free domain has a direct impact on the internal environment sensed by the molecular rotor. In RNA-rich condensates, nucleic acids act as a polymer scaffold interconnecting proteins within a meshwork containing relatively large solvent-filled spaces. Reduction of RNA content leads to smaller, denser condensates,[14] increasing the probability of rotor−protein collisions. Consequently, the viscosity measured in ActD-treated nucleoli is higher than in untreated, rRNA-rich nucleoli. Consistent with our observations, increases in nucleolar density following ActD treatment have been reported using optical diffraction tomography (ODT) and FCS.[13,14]

Comparative Analysis of Nuclear and Cytoplasmic Condensates

Finally, we wanted to explore whether the BOD-PEG4-L probe can sense the differences between cellular condensates. To this aim, we performed FLIM imaging of BOD-PEG4-L in stress granules (SG) in U2OS cells expressing Ras GTPase-activating protein-binding protein fused to HaloTag (HaloTag-G3BP1).[27] G3BP1 is a major protein orchestrating the assembly of the SG.[47] The latter are formed as a response of the cell to harsh environmental conditions such as oxidative and thermal stress or the presence of pathogens, when the cell induces a translational arrest in which cellular mRNA and RNA-binding proteins concentrate in these liquid-like droplets.[48]

U2OS cells expressing HaloTag-G3BP1 were treated with sodium arsenite to induce oxidative stress, labeled, and imaged by FLIM (Figure 6A). The average fluorescence lifetime measured in the stress granules was 1.45 ns, corresponding to a low apparent viscosity ~2.1 mPa·s (Figure 6B, Figure S33, Table S7) which is comparable to values measured for free HaloTag in the cell cytoplasm (Figure 3). The apparent microviscosity in the SG was about 3.5 times lower as compared to the cell nucleolus. This result indicates that the RNA/protein network in the SG is sparse compared to the nucleolus and contains larger free spaces.

In order to verify this difference, U2OS cells were cotransfected with NPM-HaloTag or HaloTag-G3BP1 together with plasmids coding for eGFP or an eGFP trimer (eGFP3). The cells were labeled with JF650-Halo ligand, imaged by confocal microscopy, and the partition coefficient of eGFP and eGFP3 in both MLOs was quantified by measuring the ratio of eGFP fluorescence intensity inside vs outside. Since eGFP monomer and trimer are not supposed to interact with the cellular structures, their diffusion within the MLOs in the cell is limited only by their size relative to protein/RNA meshwork

Downloaded from pubs.acs.org/cbihbp/article-pdf/doi/10.1021/cbmi.6c00048/6090427/cbmi.6c00048.pdf by guest on 07 September 2026

https://doi.org/10.1021/cbmi.6c00048
Chem. Biomed. Imaging XXXX, XXX, XXX−XXX

density and permeability; hence, the partition coefficient is a measure of permeability of the MLOs for each protein. eGFP and eGFP3 were found to be excluded from the nucleolus. The partition coefficient value of eGFP in the nucleolus was 0.7 and decreased to 0.6 for eGFP3. This observation indicates that the nucleolus is a relatively dense condensate since the monomeric eGFP with a hydrodynamic radius approaching 2.5 nm[49] is excluded. In contrast, both eGFP and eGFP3 penetrated stress granules. The partition coefficient was close to unity for eGFP and decreased slightly to 0.9 for the eGFP3 trimer, indicating the presence of much larger accessible free spaces within the stress granules.

Our results align with ODT analyses by Kim et al., who showed that SGs provide minimal refractive-index contrast relative to the cytoplasm, indicating a low concentration of SG components.[14] In line with this, single-molecule tracking of G3BP1 performed by Niewidok and coworkers revealed the presence of immobile dense nanocores (100−200 nm), surrounded by a more fluid phase in which proteins remain highly mobile.[27] Our results thus reinforce the view that SGs represent low-density cytoplasmic condensates with a large RNA meshwork.

CONCLUSIONS

In this study, we developed a BODIPY-based molecular rotor functionalized with a HaloTag ligand for monitoring microviscosity in various cellular environments including membraneless organelles (MLOs). To this end, we optimized the BODIPY rotor with a HaloTag ligand separated by a PEG4 linker. This design provided high sensitivity to environmental viscosity, cell permeability, and efficient, specific labeling of cellular targets.

Combined with FLIM, this probe enabled the visualization of local microviscosity differences between cellular compartments, between nucleolar subcompartments, and during nucleolar reorganization induced by transcriptional inhibition. It also revealed marked differences between the nucleolus and stress granules.

Importantly, the values reported here should be interpreted as local microviscosity estimates sensed in the immediate environment of the labeled proteins. In addition, careful optimization of illumination conditions is required prior to FLIM experiments to avoid bias related to photoinduced lifetime changes.

Overall, this approach provides information complementary to existing methods used to characterize biomolecular condensates. Given the key importance of rheological properties in MLO functions, the use of molecular rotors expands the experimental toolbox available to investigate the physical organization of membraneless organelles in living cells.

ASSOCIATED CONTENT

Supporting Information

The Supporting Information is available free of charge at https://pubs.acs.org/doi/10.1021/cbmi.6c00048.

Detailed synthetic protocols and full characterization of all compounds, stability of HaloTag protein, time resolved anisotropy and fluorescence correlation spectroscopy measurements, phasor plots and raw fluorescence decays of cellular and viscosity calibration measurements, micro and macroviscosity measurements of PEG solutions, photostability of BOD-PEG4-L in HEK293 cells, FLIM imaging of BOD-L in cells, and localization of NPM and Fib in the nucleolar subcompartments (PDF)

AUTHOR INFORMATION

Corresponding Authors

Pascal Didier − *Laboratory of Bioimaging and Pathologies (LBP), UMR 7021, CNRS, Université de Strasbourg, Illkirch-Graffenstaden 67401, France;* orcid.org/0000-0003-2850-9186; Email: pascal.didier@unistra.fr

Mayeul Collot − *Chemistry of Photoresponsive Systems, Laboratoire de Chémo-Biologie Synthétique Et Thérapeutique (CBST) UMR 7199, CNRS, Université de Strasbourg, Illkirch 67400, France;* orcid.org/0000-0002-8673-1730; Email: mayeul.collot@unistra.fr

Halina Anton − *Laboratory of Bioimaging and Pathologies (LBP), UMR 7021, CNRS, Université de Strasbourg, Illkirch-Graffenstaden 67401, France;* orcid.org/0000-0003-1304-8671; Email: halina.anton@unistra.fr

Authors

Avantika Kapoor − *Laboratory of Bioimaging and Pathologies (LBP), UMR 7021, CNRS, Université de Strasbourg, Illkirch-Graffenstaden 67401, France*

Carla Faivre − *Chemistry of Photoresponsive Systems, Laboratoire de Chémo-Biologie Synthétique Et Thérapeutique (CBST) UMR 7199, CNRS, Université de Strasbourg, Illkirch 67400, France; INSERM (French National Institute of Health and Medical Research), UMR 1260, Regenerative Nanomedecine (RNM), FMTS, Université de Strasbourg, Strasbourg 67000, France;* orcid.org/0009-0005-6777-3600

Chloé Frey − *Laboratory of Bioimaging and Pathologies (LBP), UMR 7021, CNRS, Université de Strasbourg, Illkirch-Graffenstaden 67401, France*

Pierre Hener − *In Vitro Imaging Platform − Centre de Neurochimie, UAR 3156, CNRS/, Université de Strasbourg, Strasbourg 67000, France*

Tania Steffan − *Laboratory of Bioimaging and Pathologies (LBP), UMR 7021, CNRS, Université de Strasbourg, Illkirch-Graffenstaden 67401, France*

Thiebault Lequeu − *Laboratory of Bioimaging and Pathologies (LBP), UMR 7021, CNRS, Université de Strasbourg, Illkirch-Graffenstaden 67401, France*

Andrey S. Klymchenko − *Laboratory of Bioimaging and Pathologies (LBP), UMR 7021, CNRS, Université de Strasbourg, Illkirch-Graffenstaden 67401, France;* orcid.org/0000-0002-2423-830X

Nicolas Anton − *INSERM (French National Institute of Health and Medical Research), UMR 1260, Regenerative Nanomedecine (RNM), FMTS, Université de Strasbourg, Strasbourg 67000, France;* orcid.org/0000-0002-7047-9657

Complete contact information is available at: https://pubs.acs.org/10.1021/cbmi.6c00048

Author Contributions

A.K., C.F., P.D., and H.A. performed the spectroscopy and microscopy experiments and analyzed the data. C.F. synthesized and characterized all BODIPY derivatives used in this study. T.L. and T.S. performed the molecular biology and recombinant protein purification experiments. P.H. optimized

Downloaded from pubs.acs.org/cbihbp/article-pdf/doi/10.1021/cbmi.6c00048/6090427/cbmi.6c00048.pdf by guest on 07 September 2026

the FLIM imaging and phasor plot analysis. M.C. conceptualized and supervised the organic synthesis of the viscosity probes. N.A. performed the rheology measurements, and P.D. and H.A. supervised the fluorescence spectroscopy and microscopy experiments. P.D., N.A., M.C., A.S.K., and H.A. conceptualized the project and participated in the funding acquisitions. The original draft was written by A.K., P.D., and H.A. and was edited and validated by all coauthors.

Notes

The authors declare no competing financial interest.

■ ACKNOWLEDGMENTS

This work was funded by the French National Research Agency (ANR) FluoLLPS ANR-23-CE11-0016 and IdEx Recherche Exploratoire, Unistra (R22086MM). The authors would like to thank Imaging Center PIQ-QuESt (https://piq.unistra.fr/) and Plateforme d'imagerie "In Vitro", members of the national infrastructure France-BioImaging supported by the French National Research Agency (ANR-24-INBS-0005 FBI BIOGEN). The authors thank Dr. Éléonore Réal (Université de Strasbourg) for her valuable advice on molecular biology experiments and Dr. Patrice Rassam (Université de Strasbourg) for his expertise in protein purification.

■ REFERENCES

(1) Falahati, H.; Haji-Akbari, A. Thermodynamically Driven Assemblies and Liquid-Liquid Phase Separations in Biology. *Soft Matter* **2019**, *15* (6), 1135−1154.
(2) Hyman, A. A.; Weber, C. A.; Jülicher, F. Liquid-Liquid Phase Separation in Biology. *Annu. Rev. Cell Dev. Biol.* **2014**, *30* (1), 39−58.
(3) Boeynaems, S.; Alberti, S.; Fawzi, N. L.; Mittag, T.; Polymenidou, M.; Rousseau, F.; Schymkowitz, J.; Shorter, J.; Wolozin, B.; Van Den Bosch, L.; Tompa, P.; Fuxreiter, M. Protein Phase Separation: A New Phase in Cell Biology. *Trends Cell Biol.* **2018**, *28* (6), 420−435.
(4) Banani, S. F.; Lee, H. O.; Hyman, A. A.; Rosen, M. K. Biomolecular Condensates: Organizers of Cellular Biochemistry. *Nat. Rev. Mol. Cell Biol.* **2017**, *18* (5), 285−298.
(5) Alberti, S.; Dormann, D. Liquid−Liquid Phase Separation in Disease. *Annu. Rev. Genet.* **2019**, *53* (1), 171−194.
(6) Alshareedah, I.; Thurston, G. M.; Banerjee, P. R. Quantifying Viscosity and Surface Tension of Multicomponent Protein-Nucleic Acid Condensates. *Biophys. J.* **2021**, *120*, 1161−1169.
(7) Alshareedah, I.; Kaur, T.; Banerjee, P. R. Methods for Characterizing the Material Properties of Biomolecular Condensates. *Methods Enzymol.* **2021**, *646*, 143−183.
(8) Català-Castro, F.; Ortiz-Vásquez, S.; Martínez-Fernández, C.; Pezzano, F.; Garcia-Cabau, C.; Fernández-Campo, M.; Sanfeliu-Cerdán, N.; Jiménez-Delgado, S.; Salvatella, X.; Ruprecht, V.; Frigeri, P.-A.; Krieg, M. Measuring Age-Dependent Viscoelasticity of Organelles, Cells and Organisms with Time-Shared Optical Tweezer Microrheology. *Nat. Nanotechnol.* **2025**, *20* (3), 411−420.
(9) Jawerth, L. M.; Ijavi, M.; Ruer, M.; Saha, S.; Jahnel, M.; Hyman, A. A.; Jülicher, F.; Fischer-Friedrich, E. Salt-Dependent Rheology and Surface Tension of Protein Condensates Using Optical Traps. *Phys. Rev. Lett.* **2018**, *121* (25), 258101.
(10) Alshareedah, I.; Borcherds, W. M.; Cohen, S. R.; Singh, A.; Posey, A. E.; Farag, M.; Bremer, A.; Strout, G. W.; Tomares, D. T.; Pappu, R. V.; Mittag, T.; Banerjee, P. R. Sequence-Specific Interactions Determine Viscoelasticity and Aging Dynamics of Protein Condensates. *Nat. Phys.* **2024**, *20* (9), 1482−1491.
(11) Taylor, N. O.; Wei, M.-T.; Stone, H. A.; Brangwynne, C. P. Quantifying Dynamics in Phase-Separated Condensates Using Fluorescence Recovery after Photobleaching. *Biophys. J.* **2019**, *117* (7), 1285−1300.
(12) Muzzopappa, F.; Hummert, J.; Anfossi, M.; Tashev, S. A.; Herten, D.-P.; Erdel, F. Detecting and Quantifying Liquid-Liquid Phase Separation in Living Cells by Model-Free Calibrated Half-Bleaching. *Nat. Commun.* **2022**, *13* (1), 7787.
(13) Kim, J. K.; Lee, B.-W.; Fujii, F.; Kim, J.; Pack, C.-G. Physicochemical Properties of Nucleoli in Live Cells Analyzed by Label-Free Optical Diffraction Tomography. *Cells* **2019**, *8*, 699.
(14) Kim, T.; Yoo, J.; Do, S.; Hwang, D. S.; Park, Y.; Shin, Y. RNA-Mediated Demixing Transition of Low-Density Condensates. *Nat. Commun.* **2023**, *14* (1), 2425.
(15) Chambers, J. E.; Kubánková, M.; Huber, R. G.; López-Duarte, I.; Avezov, E.; Bond, P. J.; Marciniak, S. J.; Kuimova, M. K. An Optical Technique for Mapping Microviscosity Dynamics in Cellular Organelles. *ACS Nano* **2018**, *12* (5), 4398−4407.
(16) Ferri, G.; Nucara, L.; Biver, T.; Battisti, A.; Signore, G.; Bizzarri, R. Organization of Inner Cellular Components as Reported by a Viscosity-Sensitive Fluorescent Bodipy Probe Suitable for Phasor Approach to FLIM. *Biophys. Chem.* **2016**, *208*, 17−25.
(17) Kubánková, M.; López-Duarte, I.; Kiryushko, D.; Kuimova, M. K. Molecular Rotors Report on Changes in Live Cell Plasma Membrane Microviscosity upon Interaction with Beta-Amyloid Aggregates. *Soft Matter* **2018**, *14* (46), 9466−9474.
(18) Wu, Y.; Stefl, M.; Olzyńska, A.; Hof, M.; Yahioglu, G.; Yip, P.; Casey, D. R.; Ces, O.; Humpolíčková, J.; Kuimova, M. K. Molecular Rheometry: Direct Determination of Viscosity in Lo and Ld Lipid Phases via Fluorescence Lifetime Imaging. *Phys. Chem. Chem. Phys.* **2013**, *15* (36), 14986−14993.
(19) Kashirina, A. S.; López-Duarte, I.; Kubánková, M.; Gulin, A. A.; Dudenkova, V. V.; Rodimova, S. A.; Torgomyan, H. G.; Zagaynova, E. V.; Meleshina, A. V.; Kuimova, M. K. Monitoring Membrane Viscosity in Differentiating Stem Cells Using BODIPY-Based Molecular Rotors and FLIM. *Sci. Rep.* **2020**, *10* (1), 14063.
(20) Wei, Y.; Gao, X.; Fang, J.; Xiao, Y.; Liu, J.; Liu, Y.; Zhang, X.; Shen, B. Tailoring the PK(a) of Fluorescence Lifetime Imaging Probes to Visualize Aggrephagy and Resolve Its Microenvironmental Viscosity. *Anal. Chem.* **2024**, *96* (35), 14160−14167.
(21) Los, G. V.; Encell, L. P.; McDougall, M. G.; Hartzell, D. D.; Karassina, N.; Zimprich, C.; Wood, M. G.; Learish, R.; Ohana, R. F.; Urh, M.; Simpson, D.; Mendez, J.; Zimmerman, K.; Otto, P.; Vidugiris, G.; Zhu, J.; Darzins, A.; Klaubert, D. H.; Bulleit, R. F.; Wood, K. V. HaloTag: A Novel Protein Labeling Technology for Cell Imaging and Protein Analysis. *ACS Chem. Biol.* **2008**, *3* (6), 373−382.
(22) Saladin, L.; Breton, V.; Le Berruyer, V.; Nazac, P.; Lequeu, T.; Didier, P.; Danglot, L.; Collot, M. Targeted Photoconvertible BODIPYs Based on Directed Photooxidation-Induced Conversion for Applications in Photoconversion and Live Super-Resolution Imaging. *J. Am. Chem. Soc.* **2024**, *146* (25), 17456−17473.
(23) Wang, W.; Budhu, A.; Forgues, M.; Wang, X. W. Temporal and Spatial Control of Nucleophosmin by the Ran-Crm1 Complex in Centrosome Duplication. *Nat. Cell Biol.* **2005**, *7* (8), 823−830.
(24) Chen, D.; Huang, S. Nucleolar Components Involved in Ribosome Biogenesis Cycle between the Nucleolus and Nucleoplasm in Interphase Cells. *J. Cell Biol.* **2001**, *153* (1), 169−176.
(25) Appelhans, T.; Richter, C. P.; Wilkens, V.; Hess, S. T.; Piehler, J.; Busch, K. B. Nanoscale Organization of Mitochondrial Microcompartments Revealed by Combining Tracking and Localization Microscopy. *Nano Lett.* **2012**, *12* (2), 610−616.
(26) Guillen-Chable, F.; Rodríguez Corona, U.; Pereira-Santana, A.; Bayona, A.; Rodríguez-Zapata, L. C.; Aquino, C.; Šebestová, L.; Vitale, N.; Hozak, P.; Castano, E. Fibrillarin Ribonuclease Activity Is Dependent on the GAR Domain and Modulated by Phospholipids. *Cells* **2020**, *9*, 1143.
(27) Niewidok, B.; Igaev, M.; Pereira da Graca, A.; Strassner, A.; Lenzen, C.; Richter, C. P.; Piehler, J.; Kurre, R.; Brandt, R. Single-Molecule Imaging Reveals Dynamic Biphasic Partition of RNA-Binding Proteins in Stress Granules. *J. Cell Biol.* **2018**, *217* (4), 1303−1318.
(28) Böhm, J.; Thavaraja, R.; Giehler, S.; Nalaskowski, M. M. A Set of Enhanced Green Fluorescent Protein Concatemers for Quantitative

Downloaded from pubs.acs.org/cbihbp/article-pdf/doi/10.1021/cbmi.6c00048/6090427/cbmi.6c00048.pdf by guest on 07 September 2026

Determination of Nuclear Localization Signal Strength. *Anal. Biochem.* **2017**, *533*, 48−55.
(29) Pelletier, R.; Danylchuk, D. I.; Benaissa, H.; Broch, F.; Vauchelles, R.; Gautier, A.; Klymchenko, A. S. Genetic Targeting of Solvatochromic Dyes for Probing Nanoscale Environments of Proteins in Organelles. *Anal. Chem.* **2023**, *95* (22), 8512−8521.
(30) Tomishige, N.; Bin Nasim, M.; Murate, M.; Pollet, B.; Didier, P.; Godet, J.; Richert, L.; Sako, Y.; Mély, Y.; Kobayashi, T. HIV-1 Gag Targeting to the Plasma Membrane Reorganizes Sphingomyelin-Rich and Cholesterol-Rich Lipid Domains. *Nat. Commun.* **2023**, *14* (1), 7353.
(31) Digman, M. A.; Caiolfa, V. R.; Zamai, M.; Gratton, E. The Phasor Approach to Fluorescence Lifetime Imaging Analysis. *Biophys. J.* **2008**, *94*, L14−6.
(32) Ranjit, S.; Malacrida, L.; Jameson, D. M.; Gratton, E. Fit-Free Analysis of Fluorescence Lifetime Imaging Data Using the Phasor Approach. *Nat. Protoc.* **2018**, *13* (9), 1979−2004.
(33) Vyšniauskas, A.; López-Duarte, I.; Duchemin, N.; Vu, T.-T.; Wu, Y.; Budynina, E. M.; Volkova, Y. A.; Peña Cabrera, E.; Ramírez-Ornelas, D. E.; Kuimova, M. K. Exploring Viscosity, Polarity and Temperature Sensitivity of BODIPY-Based Molecular Rotors. *Phys. Chem. Chem. Phys.* **2017**, *19* (37), 25252−25259.
(34) Kubánková, M.; Chambers, J. E.; Huber, R. G.; Bond, P. J.; Marciniak, S. J.; Kuimova, M. K. Linker Length Affects Photostability of Protein-Targeted Sensor of Cellular Microviscosity. *Methods Appl. Fluoresc.* **2019**, *7* (4), 44004.
(35) Park, H.; Han, S.-S.; Sako, Y.; Pack, C.-G. Dynamic and Unique Nucleolar Microenvironment Revealed by Fluorescence Correlation Spectroscopy. *FASEB J. Off. Publ. Fed. Am. Soc. Exp. Biol.* **2015**, *29* (3), 837−848.
(36) Liang, L.; Wang, X.; Xing, D.; Chen, T.; Chen, W. R. Noninvasive Determination of Cell Nucleoplasmic Viscosity by Fluorescence Correlation Spectroscopy. *J. Biomed. Opt.* **2009**, *14* (2), 24013.
(37) Yang, Z.; He, Y.; Lee, J.-H.; Park, N.; Suh, M.; Chae, W.-S.; Cao, J.; Peng, X.; Jung, H.; Kang, C.; Kim, J. S. A Self-Calibrating Bipartite Viscosity Sensor for Mitochondria. *J. Am. Chem. Soc.* **2013**, *135* (24), 9181−9185.
(38) Lafontaine, D. L. J.; Riback, J. A.; Bascetin, R.; Brangwynne, C. P. The Nucleolus as a Multiphase Liquid Condensate. *Nat. Rev. Mol. Cell Biol.* **2021**, *22* (3), 165−182.
(39) Dubois, M.-L.; Boisvert, F.-M. The Nucleolus: Structure and Function. *Functional Nucleus* **2016**, 29−49.
(40) Feric, M.; Vaidya, N.; Harmon, T. S.; Mitrea, D. M.; Zhu, L.; Richardson, T. M.; Kriwacki, R. W.; Pappu, R. V.; Brangwynne, C. P. Coexisting Liquid Phases Underlie Nucleolar Subcompartments. *Cell* **2016**, *165* (7), 1686−1697.
(41) Mitrea, D. M.; Cika, J. A.; Guy, C. S.; Ban, D.; Banerjee, P. R.; Stanley, C. B.; Nourse, A.; Deniz, A. A.; Kriwacki, R. W. Nucleophosmin Integrates within the Nucleolus via Multi-Modal Interactions with Proteins Displaying R-Rich Linear Motifs and RRNA. *Elife* **2016**, No. 5, No. e13571.
(42) Phair, R. D.; Misteli, T. High Mobility of Proteins in the Mammalian Cell Nucleus. *Nature* **2000**, *404* (6778), 604−609.
(43) Pack, C.; Saito, K.; Tamura, M.; Kinjo, M. Microenvironment and Effect of Energy Depletion in the Nucleus Analyzed by Mobility of Multiple Oligomeric EGFPs. *Biophys. J.* **2006**, *91* (10), 3921−3936.
(44) Galvanetto, N.; Ivanović, M. T.; Chowdhury, A.; Sottini, A.; Nüesch, M. F.; Nettels, D.; Best, R. B.; Schuler, B. Extreme Dynamics in a Biomolecular Condensate. *Nature* **2023**, *619* (7971), 876−883.
(45) Hernandez-Verdun, D. Assembly and Disassembly of the Nucleolus during the Cell Cycle. *Nucleus* **2011**, *2* (3), 189−194.
(46) Leung, A. K. L.; Gerlich, D.; Miller, G.; Lyon, C.; Lam, Y. W.; Lleres, D.; Daigle, N.; Zomerdijk, J.; Ellenberg, J.; Lamond, A. I. Quantitative Kinetic Analysis of Nucleolar Breakdown and Reassembly during Mitosis in Live Human Cells. *J. Cell Biol.* **2004**, *166* (6), 787−800.
(47) Yang, P.; Mathieu, C.; Kolaitis, R.-M.; Zhang, P.; Messing, J.; Yurtsever, U.; Yang, Z.; Wu, J.; Li, Y.; Pan, Q.; et al. G3BP1 Is a Tunable Switch That Triggers Phase Separation to Assemble Stress Granules. *Cell* **2020**, *181* (2), 325−345.e28.
(48) Smith, J.; Bartel, D. P. The G3BP Stress-Granule Proteins Reinforce the Integrated Stress Response Translation Programme. *Nat. Cell Biol.* **2026**, *28*, 135.
(49) Terry, B. R.; Robards, A. W. Hydrodynamic Radius Alone Governs the Mobility of Molecules through Plasmodesmata. *Planta* **1987**, *171* (2), 145−157.

Downloaded from pubs.acs.org/cbihbp/article-pdf/doi/10.1021/cbmi.6c00048/6090427/cbmi.6c00048.pdf by guest on 07 September 2026

https://doi.org/10.1021/cbmi.6c00048
Chem. Biomed. Imaging XXXX, XXX, XXX−XXX